JOM, Vol. 77, No. 1, 2025
https://doi.org/10.1007/s11837-024-06904-9

TECHNICAL ARTICLE

Experimental Investigation of Temperature Field, Fusion Zone Microstructure and Mechanical Properties During Dissimilar Laser Welding of Nickel-Base Alloy and Duplex Stainless Steel

AMIR PARSIAN,[1] MOHAMMAD AKBARI,[1,2,4] ARASH KARIMIPOUR,[1,2]
MAHDI RAFIEI,[3] and MOHAMMAD MEHDI RAZZAGHI[1,2]

1.—Department of Mechanical Engineering, Najafabad Branch, Islamic Azad University, Najafabad 8514143131, Iran. 2.—Aerospace and Energy Conversion Research Center, Najafabad Branch, Islamic Azad University, Najafabad 851414313, Iran. 3.—Advanced Materials Research Center, Department of Materials Engineering, Najafabad Branch, Islamic Azad University, Najafabad 851414313, Iran. 4.—e-mail: m.akbari.g80@gmail.com

The current study delves into the dissimilar laser welding of nickel-base alloy and duplex stainless steel, specifically in circular and plate forms, using fiber laser technology. The study utilizes a design of experiments methodology, specifically employing a central composite design, to methodically evaluate how different laser welding parameters affect the properties of dissimilar welds. The methodology is the response surface methodology (RSM), allowing for a comprehensive evaluation of the effects. The study examines the influence of key welding parameters, such as laser power, welding speed, focal distance, and laser beam deviation from the joint's center, on several response variables. These variables encompass the depth of the molten pool, the weld microstructure, and its mechanical characteristics. The depth of the molten pool, on the other hand, is primarily influenced by laser power and focal distance. Notably, a transition in microstructure is observed from columnar dendrites to a cellular configuration as one moves from the fusion line towards the center of the fusion zone. In the fusion zone of the duplex base metal, an unmixed zone is identifiable in the upper segments of the fusion line. This phenomenon arises due to incomplete melting at the fusion line.

INTRODUCTION

The dissimilar laser welding of nickel-base alloys and duplex stainless steels (DSS) is a complex process that presents unique challenges due to the materials' differing thermal and mechanical properties.[1] Fiber lasers, known for their high beam quality and energy efficiency, have advanced the capabilities of welding, enabling deeper penetration and reduced thermal distortion. As highlighted by Wang and Rong,[2] optimizing welding parameters is crucial to addressing common issues such as weld defects and incomplete fusion. This optimization is vital for achieving high-quality welds, especially in the context of dissimilar metal combinations. The influence of key welding parameters, laser power, welding speed, focal distance, and beam deviation, on the weld characteristics is significant. These parameters affect the molten pool depth, which is primarily governed by laser power and focal distance. Recent research has documented the transition in microstructure from columnar dendrites to a cellular structure within the fusion zone, driven by thermal gradients and cooling rates.[3] Understanding these transitions is crucial for improving weld quality. Moreover, the formation of unmixed zones at the fusion line of DSS due to incomplete melting is a notable challenge.[4] This issue reflects the complexity of achieving a homogeneous weld in dissimilar metal welding. Li et al.[5] discussed similar challenges in machining processes, emphasizing the need for precise control over parameters to

---

(Received April 15, 2024; accepted September 19, 2024;

effectively manage thermal dynamics. To address these challenges, this study applies a central composite design within the framework of response surface methodology (RSM), which facilitates a detailed evaluation of how variations in laser parameters affect the molten pool depth, microstructure, and mechanical properties of the weld.[6,7] Additionally, advanced optimization techniques[8–11] provide valuable tools for enhancing predictive accuracy in complex processes. Techniques such as those proposed by Li et al.[12] and Wang et al.[13] further contributed to the refinement of welding processes through improved modeling and control strategies.

Duplex stainless steel 2205, known for its distinctive characteristics compared to traditional austenitic and ferritic stainless steels, has garnered significant attention across various industrial applications.[14–16] Meanwhile, nickel-base alloy, a nickel-based superalloy, has found extensive use in turbine engines, effectively addressing high-service temperature requirements. Noteworthy attributes of this alloy encompass exceptional strength, corrosion resistance, and creep properties, particularly at elevated temperatures. These attributes outperform widely utilized superalloys like Inconel 718, HY 263, and Rene 41.[17] Welding plays a pivotal role in crafting turbine components of varying complexities, especially in assembling parts within compressor sections and crucial aircraft components. A substantial body of research has been dedicated to scrutinizing the effects of diverse parameters on dissimilar welding, spanning a wide spectrum of metal combinations. These investigations aim to unravel how factors such as welding speed, laser power, beam deflection, focal length, pulse duration, and overlap coefficient impact the quality and attributes of dissimilar welds. By systematically manipulating these parameters and assessing their repercussions on resultant weld properties, researchers have strived to optimize welding processes for dissimilar metal pairings.[18,19]

Saravanan et al.[20] conducted a study to probe the combined impact of laser power and welding speed on resulting temperatures, microstructures, and mechanical characteristics of weld zones in super-duplex steel, utilizing a pulsed YAG laser. The findings demonstrated that higher heat input rates facilitated complete penetration during welding. In a distinct exploration, Baghdadchi et al.[21] delved into the effects of laser reheating on FDX 27 duplex stainless-steel (DSS) welding. Nitrogen served as a shielding gas to enhance austenite development and mitigate nitride development in DSS welds. Calliari et al.[22] and Ghorsh et al.[23] carried out experimental inquiries into butt-welding 2205 Duplex steel using an Nd:YAG laser. Their findings unveiled that, as the pulse width increased, there was a corresponding decrease in both weld strength and the width of the weld bead. Gozarganji et al.[24] studied how a nitrogen shielding gas blend affected the microstructure and hardness in the context of pulsed laser welding of 2205 DSS. They employed both light and scanning electron microscopy to scrutinize resultant microstructures. Their observations noted hardness values escalating from 280 HV in the base metal to 307 HV in the weld centerline. Nevertheless, they found that the shielding gas mixture insignificantly impacted weld hardness. Vemanaboina et al.[25] harnessed a CO_2 laser welding device to weld Inconel 625 sheets. Experimental assessments, varying the laser power parameter, revealed that selecting superior quality characteristics curtailed distortion, rendering all welding pieces defect-free. Additionally, decreasing heat input led to diminished distortion. Ahmad et al.[26] explored the joining of Inconel 625 and DSS 2205 plates and their mechanical characteristics, microstructural features, and elemental distribution. Their findings underscored the efficacy of laser beam welding in connecting these dissimilar alloys, accentuating the link between structure and comprehensive properties. Azari et al.[27] investigated the temperature distribution and microstructural changes within the welded area of the Inconel 625 superalloy. Through the investigation of assorted parameters in laser welding, the study unveiled the notable effect of augmented laser power on temperature rise, while increased nozzle distance correlated with reduced workpiece temperature. In a separate experimental endeavor, Thejasree et al.[28] focused on the influence of laser parameters on the microstructure of the welded region in Inconel 625 superalloy during laser welding. characteristics, including penetration depth and the dimensions of the top and bottom portions of the weld bead. Furthermore, they analyzed the microstructure of the fusion zone and heat-affected zone (HAZ) and assessed the tensile properties of the resulting weldments. Their findings provided valuable insights into the optimization of laser welding parameters for Inconel 718 alloy and offered a quantitative understanding of the influence of these parameters on weld quality. Corigliano et al.[29] explored fatigue performance in the laser welding of TI6AL4V/Inconel 625 alloys, and the empirical findings indicated that the welds exhibited strong fatigue resistance, confirming their quality. The thermographic approach for predicting fatigue strength aligned well with conventional method outcomes.

Razavi examined pulsed Nd:YAG laser welding of Waspaloy sheets to assess the characteristics of weld fusion zones, including microstructure, microhardness, and corrosion behavior. His findings indicated that laser welding did not alter the phase structure of the weld zone, as evidenced by XRD patterns of the weld zone and the base metal. The weld zone's hardness values were approximately 30% lower than those of the base metal, and the corrosion resistance of the weld metal notably exceeded that of the base metal. The fusion zone's microstructure was primarily dendritic, growing perpendicular to the heat transfer direction.[30]

Overall, the experimental studies reviewed in this article have shown that fiber laser welding can be an effective method for joining duplex stainless steel and nickel-base alloys. There is no comprehensive experimental design and response surface methodology to investigate the impact of fiber laser parameters on the mechanical and microstructural properties and dissimilar alloy composition by considering different thermophysical properties including temperature field, melt volume, and melt participation of dissimilar welding between DSS and nickel-base alloy. Also, this study presents a new dissimilar joint at circular path between duplex 2205 and nickel base alloy.

EXPERIMENTAL

In the current investigation, a fiber laser boasting a maximum output power of 700 W was employed to forge a connection between two dissimilar metals—DSS and nickel-base alloy. The laser power output was measured by a PRONTO-3K laser power meter. The laser welding apparatus used was the BW210 laser welding head equipped with a side nozzle, which shielded the molten pool through a flow of pure argon gas at a rate of 1.7 L/min. The nickel-base alloy workpieces, fashioned in circular geometry with a diameter of 20 mm, were positioned within circles etched onto DSS matrices. Figure 1 portrays the strategic placement of K-type thermocouples with a 1-mm diameter, located 2 mm from the center of the molten pool. These thermocouples enabled the measurement of temperature gradients in proximity to the molten pool during the welding procedure. The temperature measurement range accuracy of ± 1% for the temperature data was captured using an Advantech USB 4718 module card and subsequently recorded through LABVIEW software. The calibration of the thermocouples was performed at four target temperature reference points of 0, 100, 200, and 300°C standard hot plate instrument. For each calibration point, five measurements were recorded. Furthermore, a tempilstik with an accuracy of ± 3% of the Celsius rate was used for weld preheat according to the AWS D1.1 standard.

Table I sets out the weight percentages of the chemical composition for both DSS and nickel-base alloy. The laser welding process was executed by securely fastening the workpieces onto a fixture. Throughout the welding operation, meticulous attention was devoted to investigating the influential parameters affecting welding quality.

A laser beam at specified speeds within a 2D coordinate CNC table with 2-axis interpolation was utilized. For capturing images of the cross-sectional geometry of welds, an Olympus microscope (BX51) was employed. Metallography preparation entailed hot-mounting the samples, followed by grinding on Sic paper ranging from 150 to 1500 grit size and concluding with polishing. The surface images of the weld beads were captured using an Olympus stereoscope (SZX18). Microstructural analysis of the molten pools and base metals was carried out using a TESCAN MIRA-3rd FESEM instrument. Microhardness testing was conducted using a ZWICK micro-hardness tester, applying a 100-g load with a dwell time of 15 s. Furthermore, tensile tests on the welded samples were executed in adherence to the ASTM E8 standard using a GOTECH AI-7000 testing machine.

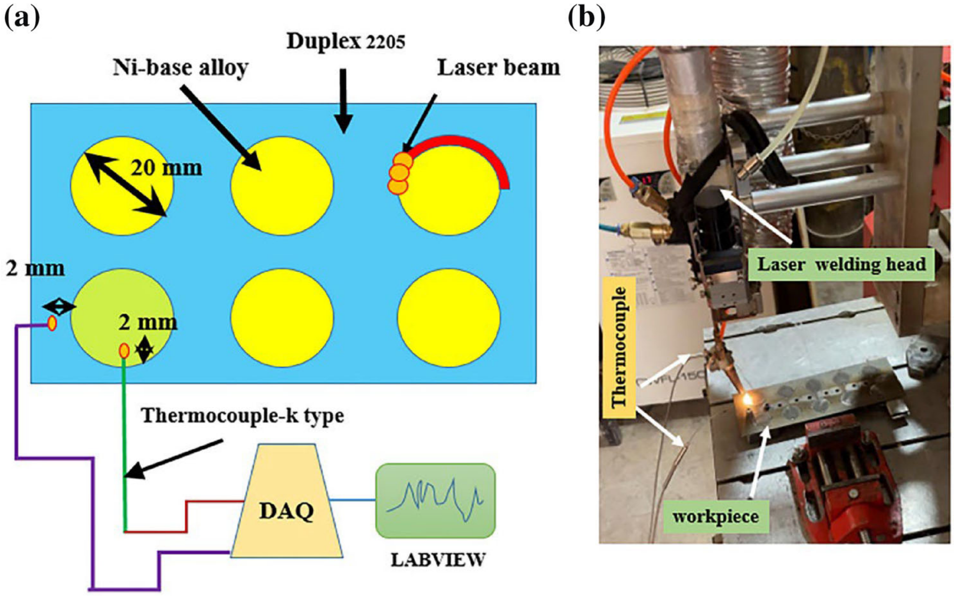

Fig. 1. Setup of laser welding experiments: (a) schematic, (b) actual view.

Table I. Chemical composition of the alloys

Element (wt.%)														
Alloy	CO	Si	Mn	P	Al	Cr	Fe	Mo	C	Ti	Zr	S	B	Ni
Nickel-base alloy	14	0.05	0.5	–	1.45	20.5	1.1	4.7	0.1	2.9	0.1	0.02	0.003	Balance
	Si	Mn	P	Al	Cr	Ni	Mo	S	C					
Duplex 2205 steel	1	2.00	0.03	0.03	23	6.5	3.5	0.02	0.03					

Table II. Selected parameters level for CCD

No	Power (W)	Velocity (mm/min)	Focal distance (mm)	Deviation (mm)
1	250–450	200–500	– 1.5 to + 4.5	– 0.5 to + 0.5

EXPERIMENTAL DESIGN

To examine the impact of various parameters on the quality of the welds, an experimental design was executed. To this end, a central composite design of experiments was adopted, incorporating four key parameters: laser intensity, welding velocity, nozzle distance, and laser beam offset. These parameters were set as input variables in the design matrix. In the preliminary stages of experimentation, the parameter ranges were determined, as outlined in Table II. The design matrix encompassed 5 central points, 8 axial points, and 16 points situated on the surfaces of a cube, totaling 29 experiments, as delineated in Table III.

Subsequently, the collected experimental data underwent variance analysis to evaluate the significance of various factors and their interactions. Following this, a nonlinear regression equation was formulated to establish a model depicting the relationship between the input parameters and the measured responses, adhering to the principles of the RSM. The total degrees of freedom amounted to 28, encompassing 10 degrees for linear and nonlinear terms, with the remaining 18 degrees allocated to error, wherein 14 degrees were assigned to the lack of fit.

When the regression model boasts a higher degree of freedom, the precision of the nonlinear regression model tends to be notably improved for estimating test outcomes. The responses examined in this study included the temperature in proximity to the molten pool for both metals, the tensile strength of the welded joint, and the depth of the molten pool.

RESULTS

This study aimed to evaluate the impact of laser welding process parameters on the quality of dissimilar weld joints using a design of experiments approach. The investigation involved assessing variations in responses, including the temperature near the molten pool of both base metals, the depth of the weld, and the tensile strength of the joint. Analysis of variance was employed to discern the most influential factors, as well as their potential interactions, on each response. Monitoring temperature during the laser welding process serves to establish the correlation between laser welding process parameters and resulting measurements. This encompasses parameters such as the geometry of the molten pool, microstructural transformations from the base metals extending to the fusion zone, and mechanical properties of the weld joint. Given the diverse physical properties of workpieces, both geometric and thermophysical, in dissimilar laser welding, the resultant temperature gradient during the welding process can significantly impact weld quality factors. Regression models, constructed using experimental data, emerge as potent tools for predicting outcomes with considerable accuracy.

Effects of Process Parameters on the Dissimilar Joint Formation

The effect of laser welding parameters on the variation of the weld bead characterizations is illustrated in Fig. 2. The welding speed, laser power, and focal distance effect on the weld bead surface appearance were evaluated. As can be seen in Fig. (2a–c), by increasing the focal distance to about 3 mm, the volume of the melted material reduced and the surface of the weld bead changed from concave to flat when the focal distance increased and laser beam energy density reduced. The width of the weld bead clearly increased by about 20% by increasing the beam diameter. In contrast, the actual weld bead width slightly diminished when the focal distance increased from 1.5 mm to 3 mm because of decreasing the laser beam energy density of about 0.9 W/cm^2. Hence, the weld width decreased by about 15%. Figure 2d–f illustrates the effect of increasing the laser power on the weld bead width and surface topography. By increasing the laser power from 300 W to 400 W, the

Table III. Laser welding parameters and their levels by CCD design

No	Power (W)	Velocity (mm/min)	Focal distance (mm)	Deviation (mm)
1	350	300	1.5	0.00
2	300	200	0.0	– 0.25
3	350	500	1.5	0.00
4	400	200	0.0	– 0.25
5	350	300	1.5	0.00
6	300	400	0.0	– 0.25
7	300	400	0.0	0.25
8	350	300	1.5	0.50
9	450	300	1.5	0.00
10	400	400	3.0	– 0.25
11	400	200	3.0	– 0.25
12	250	300	1.5	0.00
13	400	200	3.0	0.25
14	350	300	1.5	0.00
15	300	200	3.0	0.25
16	400	400	0.0	0.25
17	350	300	1.5	– 0.50
18	350	300	1.5	0.00
19	350	300	– 1.5	0.00
20	300	400	3.0	0.25
21	300	400	3.0	– 0.25
22	350	300	4.5	0.00
23	350	300	1.5	0.00
24	400	400	0.0	– 0.25
25	400	200	0.0	0.25
26	300	200	0.0	0.25
27	400	400	3.0	0.25
28	350	100	1.5	0.00
29	300	200	3.0	– 0.25

width of the weld bead increased by a remarkable 80%. Additionally, the weld bead surface became more concave by increasing the laser power from 250 W to 350 W. Evidently, augmentation of laser power from 350 to 450 W caused the laser melt volume and thereby larger weld bead width, while the weld bead surface concavity slightly reduced. Due to the higher temperature and greater flow rate of the melted material, phenomena like spattering and plasma plume have created a wider weld bead at a higher temperature which has impacted on increasing the solidification time of the melted material. The high-temperature affected area (see Fig. 2f) is clearly seen adjacent to the weld bead on both side of the two different Nickel-base alloy and DSS. The effect of decreasing welding speed on the weld bead appearance is observed in Fig. 2g–i.

The Effect of Laser Parameters on the Depth of the Molten Pool

The outcomes of the ANOVA analysis for melt pool depth, as presented in Table IV, underscore that the primary factors influencing the depth of the molten pool in dissimilar welding are laser power and focal distance. Notably, the values of Rsq (90.9%) and lack of fit (0.296) signify a strong alignment between the experimental data and the nonlinear regression model, confirming the robustness of the outcomes. Within the spectrum of other parameters, the interaction between the two variables, laser power and focal distance, emerges as the most influential on the depth of the molten pool. This finding is consistent with the tendency for laser power levels to correlate with the depth of the molten pool. This correlation arises from the fact that the heat transfer coefficients of the two alloys are closely aligned. As a result, alterations in process parameters influence the temperature formed around the molten pool and the penetration depth of the laser beam. This behavior exhibits similarity in both materials. The regression Eq. 1 encapsulates the relationship between the penetration depth of the molten pool and parameters. This equation encapsulates both linear and non-linear terms, alongside interactions between the parameters.

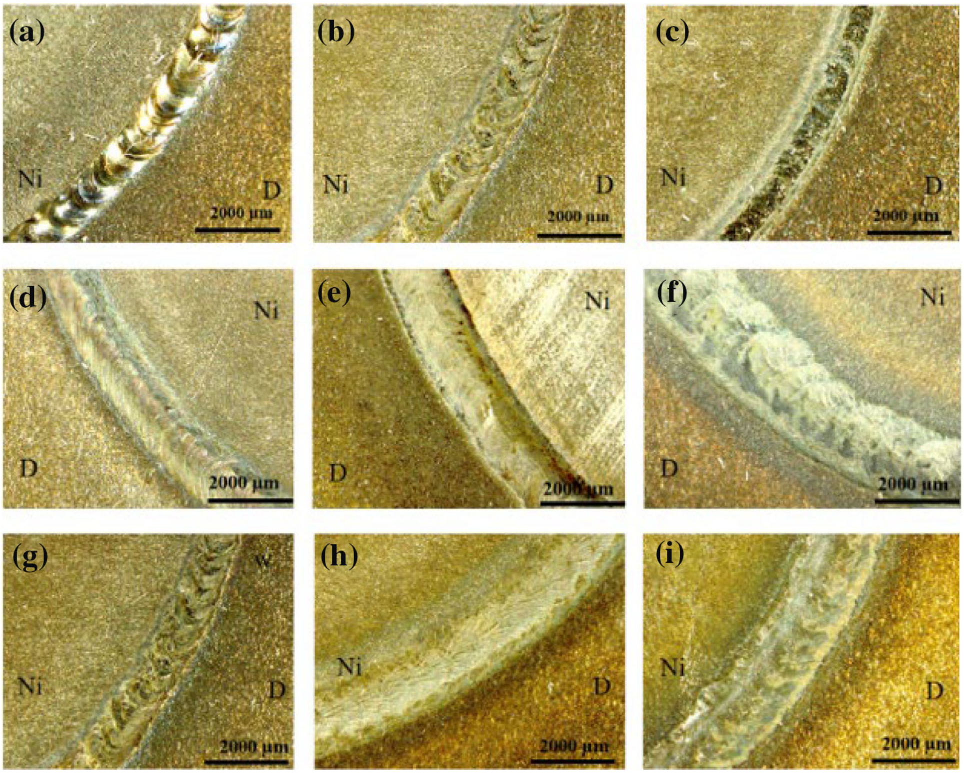

Fig. 2. The weld bead appearance (laser power 400 W, welding speed 300 mm/min) at different focal distance of (a) 0 mm, (b) 1.5 mm, (c) 3 mm (focal distance 0 mm, welding speed 300 mm/min) at different laser powers of (d) 300 W, (e) 350 W, and (f) 450 W, (laser power 400 W, focal distance 0 mm) at different welding speeds of (g) 400 mm/min, (h) 300 mm/min, and (i) 200 mm/min.

Table IV. ANOVA results for the depth of the melt pool

Source	*df*	Adj. SS	Adj. MS	*F* value	*p* value
Model	13	101,422	7801.7	21.79	0.000
Linear	4	81,600	20,400.1	56.98	0.000
Power (W)	1	42,842	42,841.5	119.65	0.000
Speed (mm/min)	1	18,481	18,481.5	51.62	0.000
Focal distance (mm)	1	7211	7210.7	20.14	0.000
Deviation (mm)	1	13,067	13,066.7	36.49	0.000
Square	3	8628	2875.9	8.03	0.002
Power (W) × power (W)	1	8045	8044.8	22.47	0.000
Focal distance (mm) × focal distance (mm)	1	68	67.6	0.19	0.670
Deviation(mm) × deviation (mm)	1	362	361.6	1.01	0.331
2-Way interaction	6	11,194	1865.6	5.21	0.004
Power (w) × speed (mm/min)	1	10,712	10,712.2	29.92	0.000
Power (w) × focal distance (mm)	1	25	25.0	0.07	0.795
Power (w) × deviation (mm)	1	100	100.0	0.28	0.605
Speed (mm/min) × focal distance (mm)	1	182	182.2	0.51	0.487
Speed (mm/min) × deviation (mm)	1	110	110.3	0.31	0.587
Focal distance (mm) × deviation (mm)	1	64	64.0	0.18	0.678
Error	15	5371	358.1		
Lack of fit	11	4704	427.6	2.57	0.188
Pure error	4	667	166.7		
Total	28	106,793			

S	R-sq	R-sq(adj)	R-sq(pred)
18.9223	94.97%	90.61%	75.18%

$$
\begin{aligned}
\text{Depth(mm)} = {} & 0.292 + 0.003433\,\text{power(W)} \\
& -0.001150\,\text{speed} - 0.519\,\text{focal distance} \\
& + 1.13\,\text{deviation} - 0.0265\,\text{focal distance} \\
& \times \text{focal distance} - 0.635\,\text{deviation} \\
& \times \text{deviation} + 0.001400\,\text{power} \\
& \times \text{focal distance} - 0.00390\,\text{power} \\
& \times \text{deviation} + 0.00180\,\text{speed} \times \text{Deviation} \\
& - 0.1867\,\text{focal distance} \times \text{deviation}
\end{aligned}
\tag{1}
$$

$$
\begin{aligned}
\text{Tensile strength (MPa)} = {} & 100.0 + 0.6400\,\text{power (W)} \\
& -0.1700\,\text{speed (mm/min)} \\
& + 5.0\,\text{focal distance (mm)} \\
& + 219\,\text{deviation (mm)} \\
& + 1.23\,\text{focal distance (mm)} \\
& \times \text{focal distance (mm)} \\
& -145.8\,\text{deviation (mm)} \\
& \times \text{deviation (mm)} \\
& -0.0500\,\text{power (W)} \\
& \times \text{focal distance (mm)} \\
& -0.700\,\text{power (W)} \\
& \times \text{deviation (mm)} \\
& + 0.195\,\text{speed (mm/min)} \\
& \times \text{deviation (mm)} \\
& -16.00\,\text{focal distance (mm)} \\
& \times \text{deviation(mm)}
\end{aligned}
\tag{2}
$$

Figure 3 shows the impact of laser power and focal distance on the depth of the molten pool. Notably, escalating the laser power from 250 W to 400 W coincides with an augmentation in the molten pool's depth, expanding from 0.5 mm to 1.5 mm. The most pronounced rate of depth increase in the molten pool was at a focal distance of 4 mm. Intriguingly, executing the welding process at the focal point and focal distance of 2 mm yielded minimal influence on the rate of depth augmentation in the molten pool.

In Fig. 4, the effect of the two parameters of laser power and welding speed on the depth of the molten pool can be seen. In general, by increasing the laser power up to 400 W, the depth of the molten pool reaches 1.5 mm. Changes in the welding speed do not have much effect on the changes in the depth of the molten pool compared to the increase in laser power.

In Fig. 5, the influence of welding speed and focal distance on the depth of the molten pool is illustrated. Notably, as the welding speed escalates from 200 mm/min to 500 mm/min at the center of the molten pool, the depth of the melt pool diminishes by approximately 0.3 mm. A noteworthy observation emerges when the focal distance is augmented from the focal point to 4 mm. At a welding speed of 200 mm/min, this leads to a reduction of about 1 mm in the depth of the molten pool. It becomes evident that elevating the welding speed triggers an overall reduction in the total depth of the molten pool. As for the impact of focal distance, an increase from the focal point to 4 mm ushers in a decrease in the molten pool's depth, which is attributed to a drop in the laser beam's energy density and an enlargement of its diameter. Consequently, the maximum

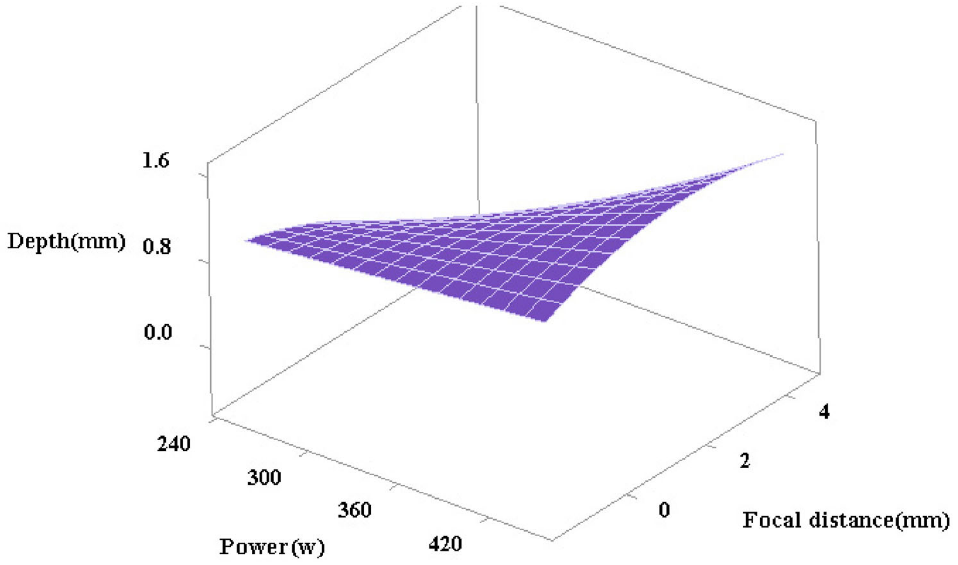

Fig. 3. The effect of laser power and focal distance on the depth of the molten pool.

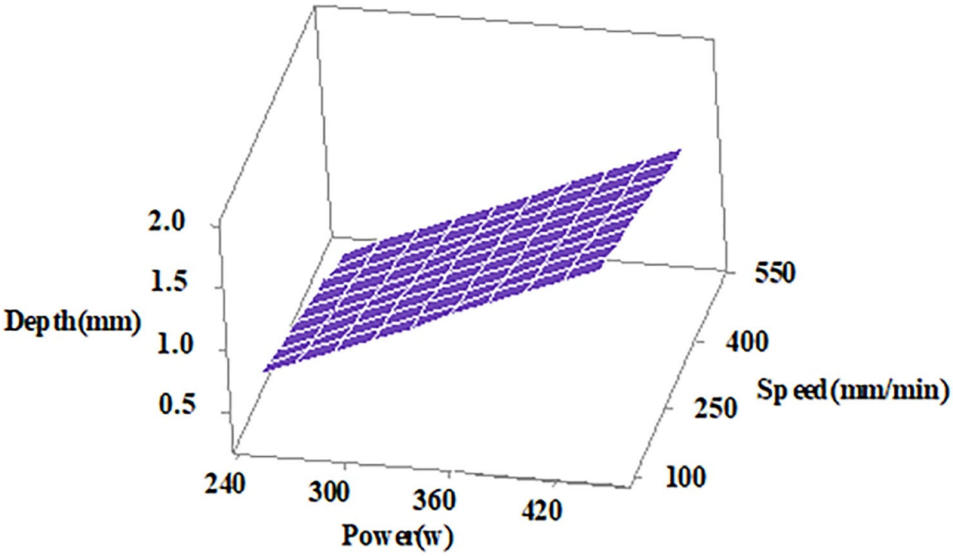

Fig. 4. The effect of laser power and welding speed on the depth of the molten pool.

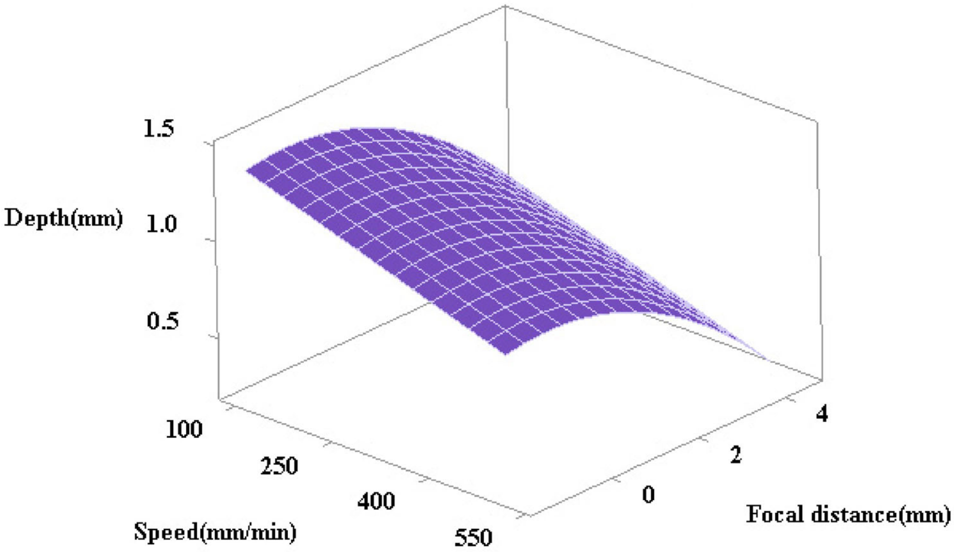

Fig. 5. The effect of welding speed and focal distance on the depth of the molten pool.

penetration depth of the molten pool diminishes. Conversely, when the focal distance is elevated from 2 mm to 4 mm, the depth of the molten pool contracts by approximately 0.8 mm. This decrease is attributed to the reduction in energy density of the laser beam, particularly at a speed of 200 mm/min.

The mechanical attributes of a welded joint hold profound significance in determining the overarching structural integrity and dependability of the welded components. The interplay between the laser parameters, including power, welding speed, focal point configuration, and beam intensity, directly impinges upon the microstructure, grain morphology, and material traits of the weld. Notably, elevated laser power and reduced welding speeds often precipitate more profound material penetration, thereby modifying heat input and cooling rates. This, in turn, exerts an influence on grain growth and the dynamics of solidification. The judicious selection and optimization of these laser parameters constitute the linchpin to achieving the coveted equilibrium between mechanical robustness, resilience, and malleability in the welded joints. An intimate comprehension of the intricate interrelationship between laser parameters and mechanical properties holds the utmost importance in the creation of welds that impeccably satisfy the exacting requisites of diverse industries, spanning from automotive and aerospace to electronics and medical devices.

Table V. ANOVA result for tensile strength of the joint

Source	*df*	Adj. SS	Adj. MS	*F* value	*p* value
Model	10	35.523.1	3552.3	16.21	0.000
Linear	4	30.371.7	7592.9	34.66	0.000
Power (W)	1	19.153.5	19.153.5	87.42	0.000
Speed (mm/min)	1	6936.0	6936.0	31.66	0.000
Focal distance (mm)	1	4160.7	4160.7	18.99	0.000
Deviation (mm)	1	121.5	121.5	0.55	0.466
Square	2	2745.2	1372.6	6.26	0.009
Focal distance (mm) × focal distance (mm)	1	210.9	210.9	0.96	0.339
Deviation (mm) × deviation (mm)	1	2291.6	2291.6	10.46	0.005
2-Way interaction	4	2406.3	601.6	2.75	0.061
Power (W) × focal distance (mm)	1	225.0	225.0	1.03	0.324
Power (W) × deviation (mm)	1	1225.0	1225.0	5.59	0.029
Speed (mm/min) × deviation (mm)	1	380.2	380.2	1.74	0.204
Focal distance (mm) × deviation (mm)	1	576.0	576.0	2.63	0.122
Error	18	3943.7	219.1		
Lack of fit	14	3372.9	240.9	1.69	0.326
Pure error	4	570.8	142.7		
Total	28	39466.8			

S	*R*-sq	*R*-sq (adj)	*R*-sq (pred)
14.8018	90.01%	84.46%	70.02%

The Effect of Laser Parameters on the Weld Joint Tensile Strength

The ANOVA results in Table V indicate that the laser power, welding speed and focal distance have the highest effect on the tensile strength of the weld by considering the value *R*-sq 90% and a lack of Fit of 0.326. The regression equation for tensile strength including linear and nonlinear terms is presented in Eq. 2.

The impact of focal distance and deviation on the tensile strength of the dissimilar joint is shown in Supplementary Figure S1 (refer to online supplementary material). The observations reveal a substantial reduction in tensile strength with an increase in focal distance, yielding the most prominent decrease of around 50 MPa when the laser beam irradiated at the joint's center. Furthermore, deviations of the laser beam towards each respective base metal result in a tensile strength decrease of up to 30% at a focal distance of 0 mm. Notably, when the laser beam deviates approximately 0.5 mm towards either base metal, a distinctive pattern emerges. This alteration leads to the creation of a deeper melt pool that extends away from the contact boundary of the two metals. Consequently, the area of fusion between the two metals diminishes, accompanied by the concurrent participation of both metals in forming the fusion zone. The influence of laser power on the tensile strength of the weld joint is elucidated concerning the laser beam deviation across both metals (see supplementary Figure S2). Notably, a distinct trend emerges as the laser power escalates and laser beam deviation is considered. Specifically, when the laser beam deviates onto the nickel-base alloy with a value of – 0.5 mm, a sharp increase in tensile strength becomes evident, surpassing that of the duplex steel or the center of the joint involving both metals. Conversely, at low levels of laser power (below 300 W), a distinctive scenario transpires. The lower absorption rate of the nickel-base alloy for the laser energy leads to diminished melting efficiency. Consequently, the fusion zone, primarily composed of the nickel-base alloy, experiences a significant reduction in volume. This results in an apparent drop of approximately 40% in the joint's tensile strength, particularly when the laser beam deviates about 0.5 mm towards the nickel-base alloy. This is particularly pronounced at laser power levels below 300 W. In the case of laser beam deviation towards the DSS, due to its higher melting point (around 100°C higher compared to the nickel-base alloy), an adequate volume of melted nickel-base alloy is present at the fusion line. Consequently, deviations of the laser beam towards the DSS exhibit minimal alteration in the weld joint's tensile strength compared to deviations towards the nickel-base alloy.

A clear comparison of the effect of laser power and welding speed on the tensile strength of the dissimilar joint is illustrated in Supplementary Figure S3. It is observed that increasing the welding speed has had a minor influence on the reduction of the tensile strength. When the welding speed increased from 100 mm/min to 500 mm/min, the tensile strength was slightly reduced and the highest amount of that was 20% at a laser power of 200 W due to incomplete melting of materials at a low laser energy line. At higher laser power levels, the reduction of tensile strength by increasing the welding speed is negligible.

A striking juxtaposition, contrasting the impact of welding speed and laser beam deviation on the tensile strength of the weld joint is depicted in supplementary Figure S4. When the laser beam is focused on the DSS side (+ 0.5 mm), the rate of reduction in tensile strength is relatively consistent with that of the center of the weld joint. In cases where the laser beam deviates towards nickel-base alloy, a conspicuous trend becomes apparent: increasing welding speed leads to a substantial threefold reduction in tensile strength compared to the center of the joint.

Consequently, at a high welding speed of 500 mm/min, when the laser beam deviates towards the nickel-base alloy, the tensile strength experiences a reduction of about 45%. This dual effect, the diminished absorption of the laser beam at higher welding speeds and the lower melting point of the nickel-base alloy, converge to drive the reduction in tensile strength within the dissimilar joint.

As illustrated in supplementary Figure S5, a clear comparison between the welded joint and base metal stress/strain behavior implies that the welded joint's ultimate stress is lower than both base metals. Although there is a difference between the ultimate stress of the duplex base metal and dissimilar joint of about 20%, for the welding process parameters condition of the center point of the CCD experimental design repeated 5 times for laser welding experiments, the ultimate tensile strength of the nickel-base alloy is clearly higher than that of the duplex base metal. Therefore, the samples are susceptive to failure from the weld joint at the duplex HAZ or duplex base metal. Additionally, as an example, when the laser power increased to more than 400 W, the tensile strength increased more and the discrepancy with the DSS tensile strength reduced more by up to 10%.

Table VI. EDS analysis results for duplex base metal and HAZ

Duplex 2205			HAZ
Element	**Point A**	**Point B**	**wt.%**
Al	–	–	0.13
Si	0.29	0.09	0.11
Ti	–	–	0.52
Cr	22.27	17.88	22.09
Mn	0.96	0.57	0.00
Fe	54.46	36.74	39.89
Co	–	–	2.74
Ni	7.73	5.88	14.92
Mo	14.05	38.84	19.29
Nb	0.23	–	0.31
Total	100	100	100

Microstructural Analysis

For the metallography analysis of the welded samples, the specimens were first cut from a cross-section of dissimilar laser-welded samples, which were prepared according to the ASTME3 standard. All the specimens were mounted in Bakelite powder by using a hot press machine and then polished from 180 to 1500 mesh grit SIC papers and finally polished by using an alumina powder suspension to achieve a mirror-like surface. A 10% oxalic acid solution was used to etch the samples followed by electro-etching with a 12-V DC power supply. The welded samples microstructure was analyzed at different zones of both base metals to the fusion zone by using an optical microscope and FESEM. Using an energy-dispersive x-ray spectroscopy (EDS) detector, the weight percentages of elements at different areas from the fusion zone to the HAZ and base metals were analyzed. A Zwick microhardness tester was used for the measurement of microhardness by applying 300 g and a time of 15 s on the weld cross-section.

Figure illustrates the microstructure and the location where EDS was performed to assess the elemental composition for both base metals of the weld joint, and Table VI presents the EDS analysis results of the points A, B, and C from the base metal and precipitated particles of the nickel-base alloy. As shown in Fig. 6b, the microstructure of the DSS consisted of dispersed austenitic grains within a ferrite matrix. Figure 6c shows the location of points where EDS was performed for the duplex 2205 steel. The nickel-base alloy base metal microstructure was composed of a nickel matrix (γ) and mainly included austenite grains, and a small number of carbide grains at the grain boundaries (see Fig. 6e). Generally, some particles with irregular shapes distributed at base metal are known as second-phase particles. Seemingly, the formation of enriched Ti, Mo, and C carbide elements occurred when cooling the equilibrium composition of liquid, γ, and MC carbides[30] according to the HAZ. The weight percentages of the elements imply that point C is rich in Ti and that C can represent MC-type carbide grains in the nickel matrix of the base metal.

Figure 7a exhibits a limited segment of the HAZ within the DSS. The microstructure within this HAZ region consists of δ ferrite grains and austenite phases, primarily initiated at the interfaces between the ferrite grains. Upon closer examination of Fig. 7a and the analysis outcomes provided by EDS (as depicted in Table VI), a noteworthy trend emerges. The microstructure within the HAZ of the DSS is primarily constituted of δ ferrite phases with heightened nickel content. This microstructural composition is a direct consequence of the higher melting point characteristic of duplex 2205 stainless steel, surpassing that of other components by approximately 100°C.

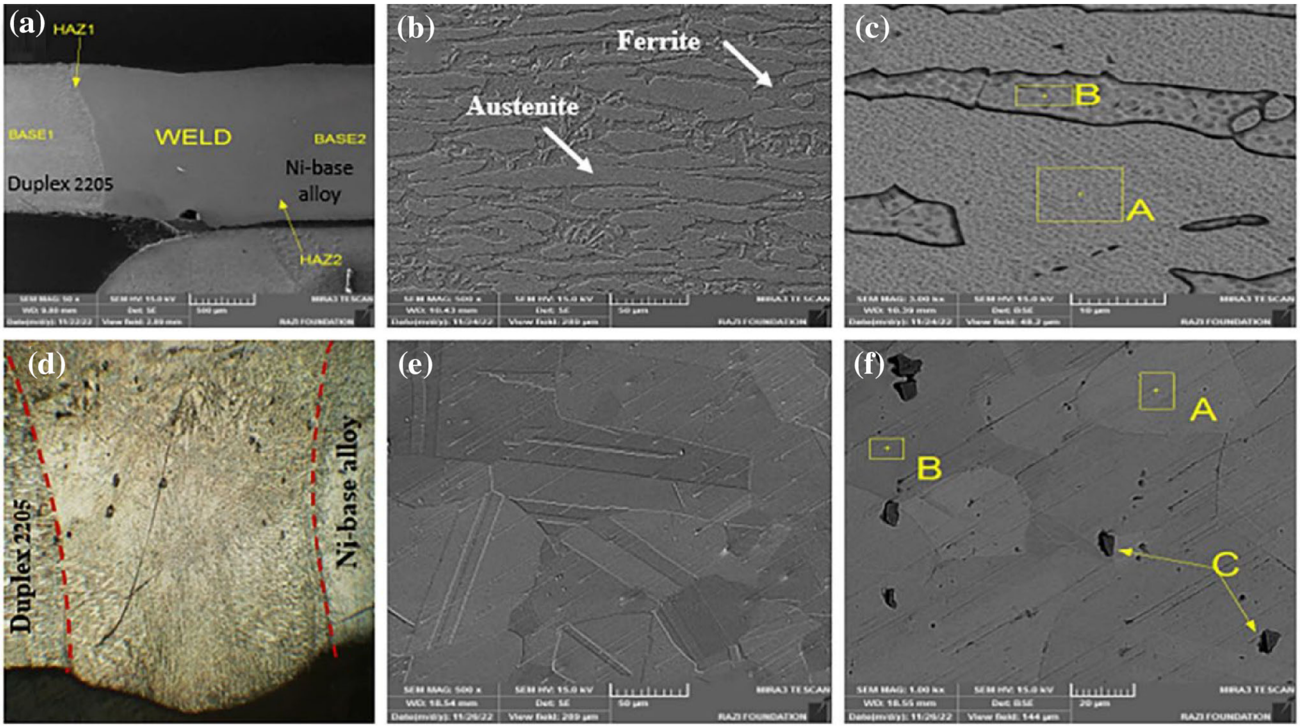

Fig. 6. SEM images of the microstructure of the weld joint and base metals for (a) weld cross-section, (b) duplex 2205 base metal, (c) duplex EDS locations, (d) optical microscope image, (e) nickel-base alloy base metal, (f) nickel-base alloy EDS locations.

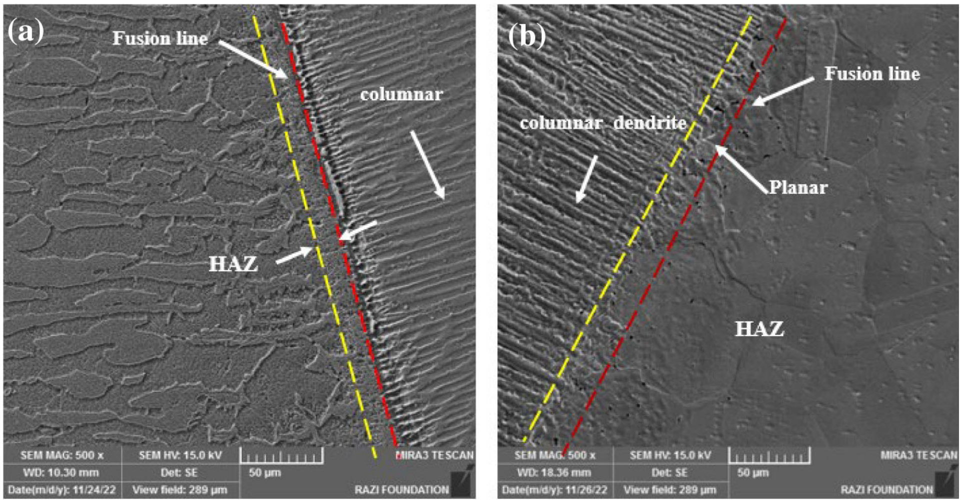

Fig. 7. SEM image of the HAZ microstructure for (a) duplex side, (b) nickel-base alloy side.

Owing to this elevated melting point, only a restricted area of the HAZ experiences minor adjustments in its microstructure. This alteration is confined to a relatively narrow region due to the material's capacity to maintain its structural integrity under the thermal conditions experienced during welding. Notably, it can be inferred that incomplete melting at the fusion line gives rise to the observation of an unmixed zone situated at the upper extremities of the fusion line within the duplex base metal.

As depicted in Fig. 7b, a conspicuous grain growth phenomenon manifested within the HAZ of the nickel-base alloy base metal, distinctly influenced by the heat input from the fusion zone. This intricate process significantly alters the microstructure within the HAZ. A discernible shift in the weight percentages of Ni and Fe within the HAZ of the nickel-base alloy is also apparent, as highlighted in Table VII. Specifically, there is a marked increase in Fe content, accompanied by a discernible reduction in Ni content.

Table VII. EDS analysis results for nickel-base alloy base metal and HAZ

Nickel-base alloy	Point A	Point B	Point C	HAZ
Element	wt.%			
Al	1.29	1.14	1.14	0.52
Si	0.09	0.07	0.07	0.07
Ti	2.80	2.66	2.66	1.64
Cr	19.02	19.02	19.02	19.74
Mn	–	0.00	0.00	0.00
Fe	0.68	0.68	0.68	23.07
Co	12.50	12.78	12.78	7.34
Ni	56.81	57.11	57.11	33.17
Mo	6.80	6.55	6.55	14.34
Nb	–	–	–	0.11
Total	100	100	100	100

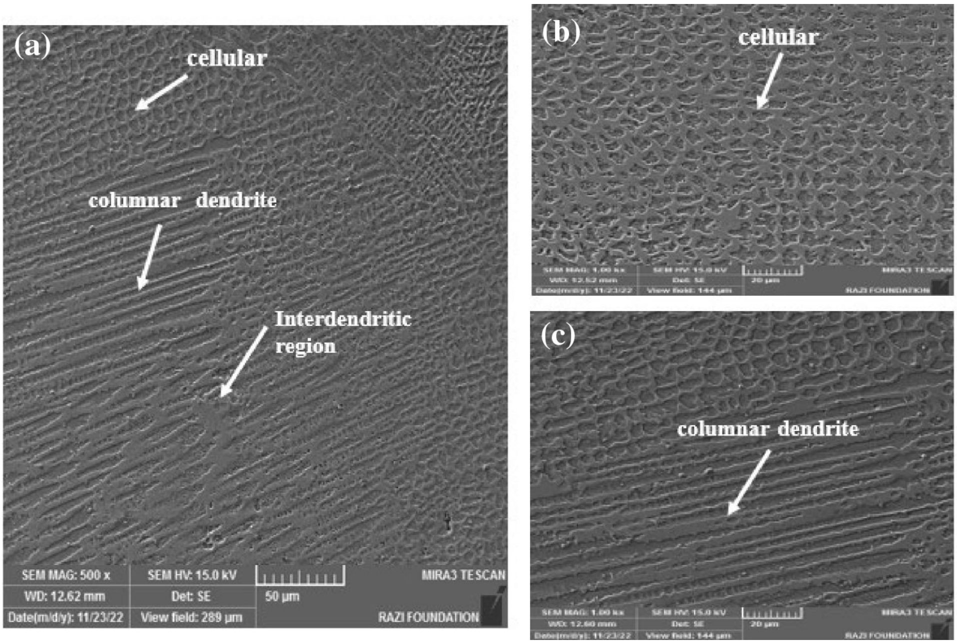

Fig. 8. SEM images of the fusion zone microstructure for (a) near the nickel-base alloy side, b) at the weld center, and (c) near the fusion line.

Further, Fig. 7b shows a comprehensive representation of the various microstructural changes occurring within the nickel-base alloy, extending from the fusion line to the weld center. Within the region inside the fusion line adjacent to both base metals, the dominant microstructure consists of columnar dendrites, which can be attributed to the rapid solidification and high cooling rates at the interface between the melt pool liquid and the solid structure of the base metals. These columnar dendrites grow perpendicular to the fusion zone boundary, originating from both base metals and progressing towards the heat transfer direction.

Figure 7b shows a distinct microstructural phase termed “planar growth” that surfaces in a narrow region immediately following the fusion line within the nickel-base alloy base metal. This is succeeded by subsequent grain growth, transitioning into dendritic growth. Throughout the welding process, the variability in the fusion zone microstructure across different regions hinges upon several factors, including the solidification rate (R), temperature gradient (g), and alloy composition.

Figure 8a elucidates the sequence of microstructural transformations within the melt pool, encompassing dendritic, interdendritic, and cellular grain growth in distinct regions. With increasing distance from the fusion line, a notable shift occurs towards cellular-shaped predominant grain growth compared to the dendritic microstructure, particularly in proximity to the weld fusion line (as observed in Fig. 8b and c).

Figure 9 depicts the points A, B, C, and D in the weld fusion zone where EDS analysis was carried

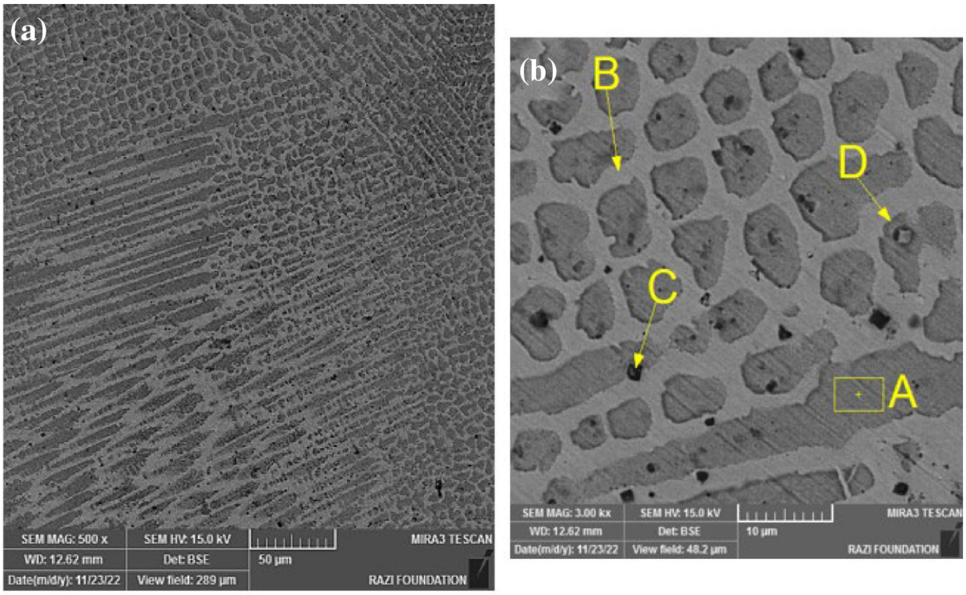

Fig. 9. Microstructure of (a) fusion zone, (b) location of EDS analysis at weld center.

Table VIII. EDS analysis results of the weld fusion zone at points

Weld area	Point A	Point B	Point C	Point D
Element	**wt.%**			
Al	0.24	0.66	–	0.45
Si	0.03	0.27	–	0.15
N	–	–	20.77	–
Ti	0.50	2.03	30.95	6.50
Cr	19.24	21.29	7.58	16.55
Mn	–	0.21	–	–
Fe	28.15	26.94	9.11	23.20
Co	6.63	6.53	2.12	5.03
Ni	29.79	32.29	10.53	24.46
Mo	15.42	9.78	4.56	6.31
C	–	–	14.39	17.34
Total	100	100	100	100

out. The EDS results in Table VIII show that there was no significant difference in the chemical composition of the interdendritic and dendritic regions of the fusion zone. According to the EDS analysis of points C, and D, some carbides, like Ti, Mo, and C, could exist in the particles known as the MC carbide. These MC carbides also existed at both the weld fusion zone and base metal.

Line scan EDS analysis offers insights into the variations in element weight percentages across both the base metals and the fusion zone. As illustrated in Fig. 10b, a comprehensive overview of the graph implies a conspicuous contribution from the nickel-base alloy in the formation of the fusion zone. This contribution is particularly evident when comparing it to the DSS base metal. Upon closer examination, several noteworthy trends emerge. The percentage of the Ni element experiences a significant decline of approximately 40% within the fusion zone. Conversely, the percentage of Fe demonstrates a more substantial reduction, surpassing 50% in comparison to the DSS base metal. Meanwhile, the chromium (Cr) element exhibits a minor shift within the fusion zone, displaying relatively modest changes in comparison to other elements. On the other hand, the cobalt (Co) element demonstrates a distinct participation in the formation of the fusion zone. Although the weight percentage of Co experiences a reduction in relation to the percentage within the nickel-base alloy base metal, it still plays a discernible role within the fusion zone.

Microhardness testing was conducted across different regions, spanning from the base metals to the weld center, to investigate the variations in hardness corresponding to distinct microstructural changes. As depicted in Fig. 11, the nickel-base alloy base metal exhibits an average microhardness of approximately 350 HV, whereas the DSS registers around 270 HV. Upon entering the HAZ of the nickel-base alloy, a reduction in microhardness to 280 HV is observed, attributed to the phenomenon of grain coarsening in this region. Upon transitioning to the fusion zone, a notable increase in microhardness occurs, reaching up to 430 HV. This heightened microhardness can be attributed to the formation of dendrites in various regions within the fusion zone. In proximity to the fusion line of the DSS, the microhardness remains relatively elevated due to dendritic growth at the fusion line. Subsequently, the microhardness experiences a sharp decline, eventually converging to the microhardness value of the DSS base metal, which stands at approximately 250 HV. The observed variations in

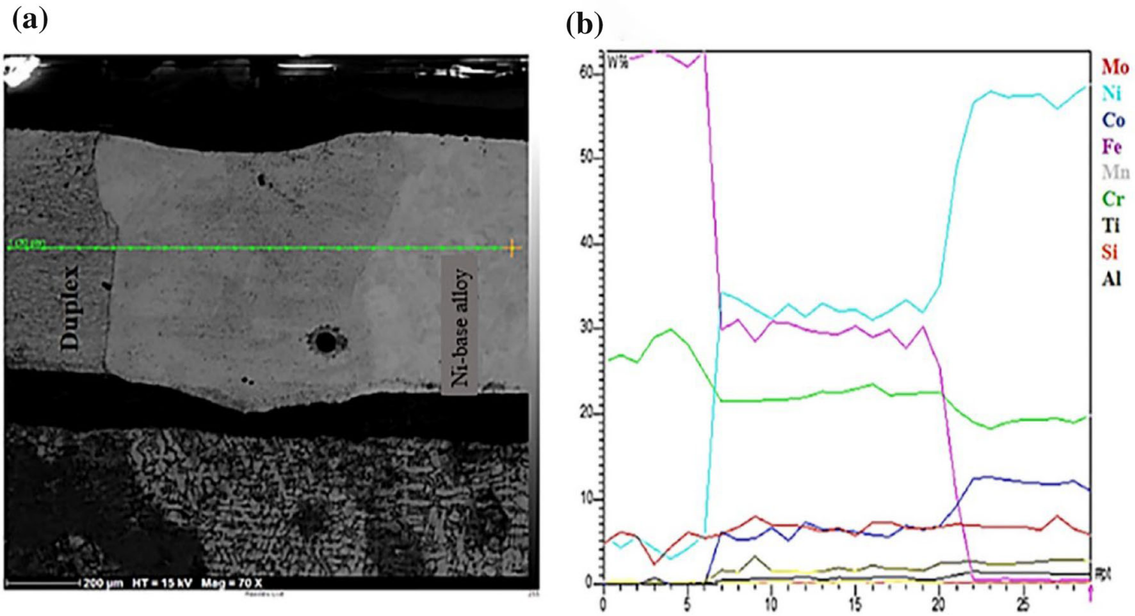

Fig. 10. Line scan analysis results for (a) locations from base metal to the weld centerline, (b) EDS analysis results.

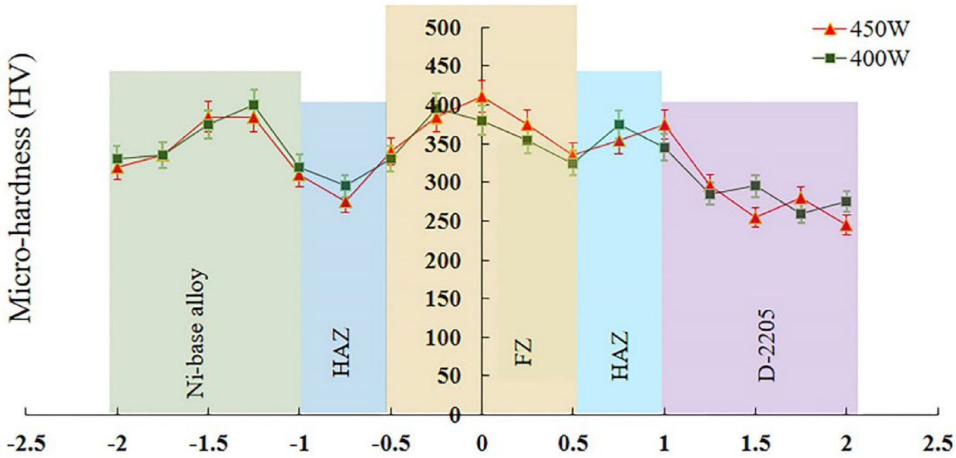

Fig. 11. Average microhardness across the weld joint from base metals to the fusion zone at a distance of 0.3 mm from the top surface and welding speed 200mm/min, focal distance 0 mm and laser powers of 400 and 450 W.

microhardness values across the fusion zone are likely linked to the diverse microstructures present and the random distribution of carbide particles within this region. Interestingly, the utilization of a higher laser power of 450 W yields minimal effects on the microhardness values. However, this does lead to a higher average hardness within the fusion zone, coupled with reduced hardness at the HAZ of the nickel-base alloy due to more extensive grain coarsening in the alloy. Furthermore, the highest microhardness observed at the center of the fusion zone can be ascribed to the elevated cooling rate, ascribed to a higher solidification rate and the presence of finer dendrite arms.[31] Similarly, the elevated hardness in the nickel-base alloy HAZ region adjacent to the base metal results from a higher temperature gradient, leading to increased cooling rates and consequently a finer microstructure.[30]

In addition, the failure mode of the welded samples was investigated in addition to their tensile strength. Tensile tests were conducted for each test condition with three repetitions, focusing on the impact of the laser power and focal distance on the tensile strength. The experiments were carried out at a specific speed of 2 mm/min. As shown in supplementary Figure S6, the visual appearance of the detached tensile test samples indicates that the failures occurred predominantly in the weld fusion zone, the fusion line of the DSS, and the HAZ of the DSS. Despite the lower mechanical strength of the DSS compared to the nickel-base alloy, the majority of the sample failures occurred in the weld fusion zone and the fusion line of the DSS. Samples welded using higher laser energy (e.g., a laser power of 400 W, welding speed of 200 mm/min, and focal distance of 0 mm) exhibited finer dendritic grains in the microstructure of the weld fusion zone and a greater depth of the melt pool. This led to higher tensile strength, a phenomenon consistent with findings from other studies.[32] Consequently, the samples primarily failed in the fusion line or the HAZ of the DSS, as shown in supplementary Figure S6(a). As observed in other data (not provided here), the microhardness of the welded samples decreases significantly as one moves from the center of the fusion zone towards the DSS. Tensile test samples tended to fail in this region despite the use of a high laser power and achieving a deeper fusion zone. A sample failure from the fusion zone near the nickel-base alloy at a focal length of 3 mm is illustrated in supplementary Figure S6(b), while adjusting the focal length from the focal point reduced the laser line energy and thereby the welded sample failure from the region near the HAZ of the nickel-base alloy.

For samples welded at lower laser power levels (e.g., 400 W), a welding speed of 200 mm/min, and focal distances of 4 and 6 mm, the failures occurred in the fusion zone (supplementary Figure S6(c, d)). With reduced laser energy, the volume of the melt pool decreased, resulting in clear observations of failures adjacent to the fusion zone of the DSS. Notably, none of the welded tensile test samples failed in the fusion line or HAZ of the nickel-base alloy. This can be attributed to the composition of the fusion zone materials, which are primarily derived from the nickel-base alloy base metal, known for its higher tensile strength compared to the DSS.

The images from the section of tensile test failure samples are shown in Fig. 12. The images of the nickel-base alloy side are shown in Fig. 12a–d and the duplex side are illustrated in Fig. 12e–h. As can be clearly observed in Fig. 12a and b, both of the samples fail from the fusion zone toward the duplex side. Figure 12a shows a ductile mode of fracture with numerous dimples distributed along the failure surface area, and some deeper cavities. In contrast, Fig. 12e shows the failure surface of the DSS which has limited number of dimples with less ductile mode, although the cavities are larger compared to the nickel-base alloy side shown in Fig. 12a. By increasing the focal length to 3 mm, the ductile mode of fracture at the nickel-base alloy side existed, while no significant number of dimples was observed for either the nickel-base alloy or the duplex side (see Fig. 12b, f). Further increasing the laser power remarkably changed the mode of fracture for the nickel-base alloy from ductile to brittle (see Fig. 12c, d). When the focal length increased to 4 mm, the fracture mode clearly seems more brittle with deeper cavities on the nickel-base alloy side (see Fig. 12c). As can be seen in Fig. 12d, a further increase of the focal length created shallower cavities on the nickel-base alloy side compared to the duplex side. It can be clearly seen in Fig. 12g, h, that the mode of fracture is brittle for the duplex side by considering the evidence that no significant changes were created on the duplex cross-section compared to the nickel-base alloy side. Hence, it can be concluded that, by welding at a high laser energy density at a focal distance of 0 mm, deeper cavities and a larger number of dimples in the ductile mode were created for the nickel-base alloy. Further increase of the focal length to 4 mm changed the

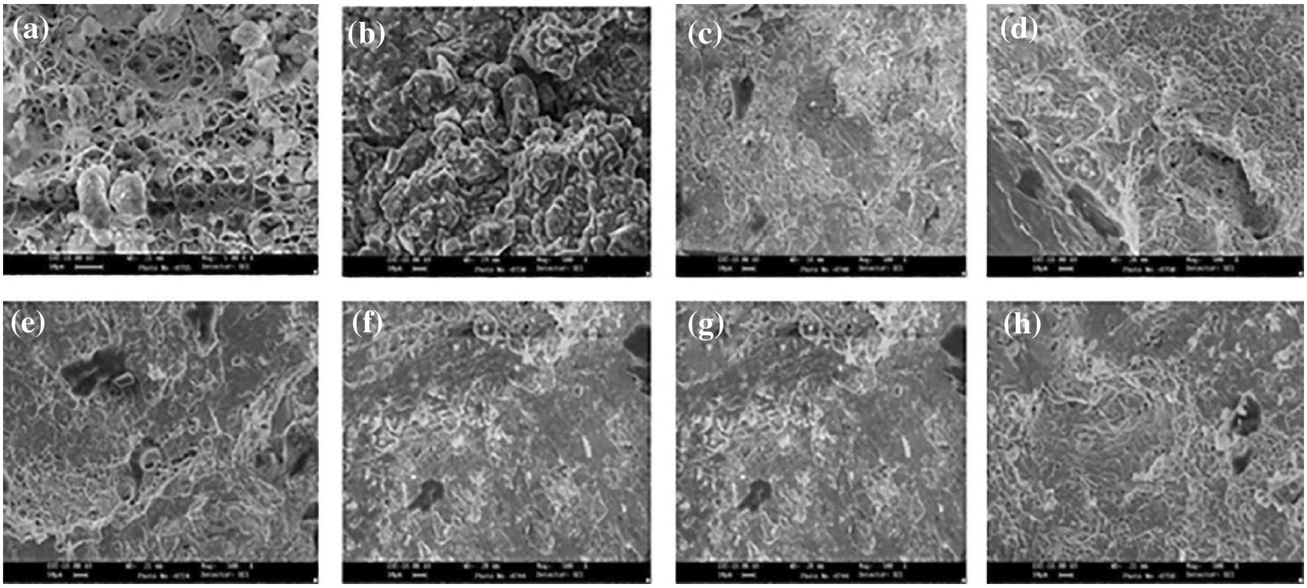

Fig. 12. Weld samples fracture section of tensile test samples for the nickel-base alloy side for the laser power of 400 W and welding speed of 200 mm/min at the center of the workpiece at focal lengths of (a) 0 mm, (b) 3 mm, (c) 4 mm, and (d) 6 mm, and for DSS side for (e) 0 mm, (f) 3 mm, (g) 4 mm, and (h) 6 mm.

mode of fracture from ductile to brittle for the nickel-base alloy side, while there were no significant changes in the failure mode of the duplex side.

DISCUSSION

Weld Bead Geometry

In this study, dissimilar laser welding of the nickel-base alloy and DSS was conducted experimentally to assess the effect of the laser welding process on the weld characterizations. The relation between laser process parameters and weld bead dimensions demonstrates that, by decreasing the welding speed, the weld bead width and the weld bead overlap percentage have been simultaneously increased. By reducing the welding speed, due to the higher interaction time of the laser beam and the workpiece, more melted material has been created, and thereby the over factor has been gradually increased because of excessive accumulation of the melted material according to the higher energy line received from the heat input. The laser power is an effective parameter to reach the proper penetration depth. By using a power level higher than 400 W, the depth of the molten pool increased by up to 1.5 mm (the total thickness of the sheet). By increasing the laser power level due to reach the full penetration depth, increasing the welding speed does not have much effect on the changes in the depth of the molten pool due to having sufficient laser line energy.

The effect of laser energy density on melt pool depth is significant. The observed behavior can be attributed to the higher energy density of the laser beam at the focal point, coupled with its proximity at 2 mm, which results in a greater molten pool depth. Consequently, the impact of elevating the laser power level, until attaining complete penetration depth, becomes less pronounced. The most substantial variance in laser penetration depth is witnessed at a focal distance of 4 mm and a power of 250 W. In this scenario, due to a noteworthy reduction in the energy density of the laser beam, the depth of the molten pool diminished by approximately 50%. With the amplification of the laser beam's energy density, the penetration depth of the laser beam was accomplished through the workpiece's thickness.

Dissimilar Joint Tensile Strength

The melt volume of the fusion zone significantly impacts the mechanical strength of the weld joint. Despite the volume of melted metals potentially remaining consistent across conditions, during the process of dissimilar laser welding, the beam deviation emerges as a pivotal factor. It plays a crucial role in achieving both the highest mechanical strength and the optimal fusion rate for both metals. The observed failure modes in the tensile test samples signify that the welded samples predominantly detach from the fusion line and the HAZ of the DSS. Comparing the welded joint and the base metal tensile strength shows that the joint tensile strength is lower than the DSS by about 20% as an average value. This difference can be reduced to 10% by selecting a higher laser power. Hence, the laser-welded dissimilar joint tensile strength has had a small difference with the DSS which can be offered for dissimilar laser welding of these alloys.

The augmentation of tensile strength according to the increase of the laser power from 250 W to 450 W was about 45%, while only about a 20% reduction was observed for increasing the welding speed.

The most significant contributors to this reduction in tensile strength are linked to the decrease in the proportion of melted volume for both metals. This phenomenon is primarily attributed to the lower absorption rate of the nickel-base alloy at higher welding speeds. The shortened interaction time between the laser beam and the substance results in a notable decrease in the melted volume of the nickel-base alloy. Compounding this, the lower melting point of the nickel-base alloy proves to be insufficient for effectively melting the DSS, especially at elevated welding speeds.

Dissimilar Joint Microstructure

The progression of microstructural transformations within the fusion zone is characterized by planar, dendritic, interdendritic, and cellular growth. This intricate evolution arises from the interplay of varied heat transfer rates across different directions, as detailed in prior research.[30]

The effect of temperature gradient on the solidification rate implies that it experiences a sharp increase moving from the fusion zone boundary adjacent to the base metal toward the weld centerline. Conversely, the temperature gradient exhibits a relatively minor decrease. This dynamic interplay of parameters engenders diverse modes of growth, shifting from planar growth at the fusion line to dendritic and cellular growth along distinct solidification grain boundaries as one traverses towards the weld centerline. The direction of the final grain growth is dictated by the maximal temperature gradient present along different directions, either parallel or perpendicular to the fusion line.

In the laser welding process, due to the rapid heating and fast cooling process, the austenite microstructure of the nickel-base alloy transformed to a dendritic microstructure, including columnar, cellular, or interdendritic microstructures at the fusion zone. As it is clearly observed in supplementary Figure S7, although the grain size of the nickel-base alloy microstructure could have the potential for measurement via EBSD methods, it is not possible to measure the dendritic microstructure grain size. Therefore, only a transformation in the microstructure of the fusion zone is observed. At the duplex side, the microstructure including ferrite and austenite transforms into a dendrite microstructure. In this case, only the percentage of ferrite to austenite could be assessed in the base metal. As a result, only the changes in microstructure from the base metals to the fusion zone could be evaluated. There is no effective way to measure the grain size of the dendrite microstructure.

The microstructure and EDS analysis of welded samples inferred that the primary constituents of the fusion zone are derived from the melting of the nickel-base alloy. In addition to the elements mentioned, molybdenum (Mo) and titanium (Ti) exhibit the most pronounced fluctuations in weight percentage within the fusion zone. This phenomenon can be attributed to the irregular distribution of particles in both the fusion zone and the nickel-base alloy base metal, leading to the formation of MC carbide particles.

Overall, the EDS analysis underscores the dominant role of the nickel-base alloy in the composition of the fusion zone, elucidating the intricate interplay of various elements during the welding process.

Future Study

Measuring the temperature and melt flow during dissimilar laser welding is of high importance. The prediction of melt flow and weld geometry via numerical simulation is a promising method. The temperature gradient at the melt pool region toward both base metals at numerous locations via numerical simulation not only effectively reduce the time and costs of the experimental procedure but also predict a dissimilar laser welding temperature field that cannot be evaluated via experimental procedures. Direct measuring of the temperature during welding because of existing different phase transformation of materials includes the solid and liquid phases and recrystallization and fusion of dissimilar materials. On the other hand, fast heating and rapid cooling cycles during laser welding cannot be effectively measured via experimental procedures.

Additionally, different thermophysical properties of the material and the laser absorbtion coefficient can increase the difficulties of temperature measurement during welding. Hence, numerical simulations of the temperature field during dissimilar laser welding, evaluation melt flow, and phase transformation and evaporation during laser welding can make a breakthrough during laser welding. Another approach could be the determining of the fusion zone grain size, orientation, and cellular–columnar dendritic transformation in the fusion zone according to the effect of temperature gradient and solidification rate on the microstructural transformation and recrystallization of the melt pool and adjacent areas using EBSD in a future study.

CONCLUSIONS

- The parameters of laser power and welding speed and laser beam deflection have the greatest effect on the temperature in the vicinity of the molten pool in the DSS and nickel-base alloy.
- Laser power and focal distance have the greatest effect on the depth of the molten pool of dissimilar welding. By using a power level higher than 400 W, the depth of the molten pool increased up to 1.5 mm (the total thickness of the sheet). By increasing the laser power due to reach the full penetration depth, increasing the welding speed does not have much effect on the changes in the depth of the molten pool due to having sufficient laser line energy.
- Laser power, welding speed, and focal distance have the highest effect on the tensile strength of the weld.
- Laser beam deviation toward the DSS does not significantly alter the weld joint tensile strength compared to the nickel-base alloy which reduced the tensile strength by about 40%.
- Inside the fusion line adjacent to both base metals, the predominant microstructure was composed of columnar dendrites. Different modes of growth from planar at the fusion line of the nickel-base alloy to the dendritic and cellular growth at different solidification grain boundaries toward the weld center line were created.
- The ESD analysis results showed that the contribution of the nickel-base alloy in the formation of the fusion zone has been evidently more than the DSS. The bulk of elements at the fusion zone were composed of Ni elements which showed the melting of the nickel-base alloy. Mo and Ti had the most weight percentage fluctuation in the fusion zone, due to the irregular distribution of particles at the fusion zone and the nickel-base alloy base metal.
- Near the fusion line of the DSS, the microhardness was relatively higher due to dendrite growth at the fusion line; after that, the hardness sharply reduced to reach the duplex value of the base metal of about 250 HV. Variations in the hardness values at different areas of the fusion zone could be related to variations in the microstructure and carbide particles randomly distributed in this region.
- The tensile test samples primarily experienced failure within the dissimilar weld fusion zone adjacent to the DSS. Microhardness assessment of the fusion zone demonstrated a clear reduction from the center of the fusion zone towards the duplex fusion line. This reduction was con-

current with a microstructural transition from cellular to dendritic in the proximity of the fusion line.

- Dissimilar laser welding of stainless-steel grades (such as duplex 2205) with high temperature and resistance to corrosion to the nickel-base material has its particular application in aero-engine parts. Applying laser welding has great potential to improve weld quality. Because of existing age cracking during current welding methods of nickel base alloys after welding, laser welding induces rapid cooling which can reduce the chance of age cracking. Furthermore, developing numerical simulations of dissimilar joints by considering different thermomechanical properties of the material could have a great potential to reduce experimental investigation costs and time.

SUPPLEMENTARY INFORMATION

The online version contains supplementary material available at https://doi.org/10.1007/s11837-024-06904-9.

COMPETING INTEREST

On behalf of all authors, the corresponding author states that there is no conflict of interest.

REFERENCES

1. Y. Zhang, M. HosseinRazaviDehkordi, M. Javad Kholoud, H. Azimy, Z. Li, and M. Akbari, *Opt. Laser Technol.* 174, 110575 (2024).
2. L. Wang, and Y. Rong, *Int. J. Hydromech.* 5(2), 167–190 (2022).
3. J. Khan, E. Lee, and K. Kim, *CAAI Trans. Intell. Technol.* https://doi.org/10.1049/cit2.12148 (2022).
4. J. Zhao, Z. Wang, and Y. Han, *Int. J. Hydromechtron.* 5(1), 44–79 (2022).
5. J. Li, T. Sui, X. Dong, F. Gu, N. Su, J. Liu, and C. Xu, *Int. J. Hydromechatron.* 5(2), 136–166 (2022).
6. N. Luo, et al., *J Data Sci Intell Syst.* https://doi.org/10.47852/bonviewJDSIS32021078 (2023).
7. J. Wang, Z. Sun, L. Gu, and H. Azimy, *Infrared Phys. Technol.* 118, 103866 (2021).
8. H. Taherdoost, and M. Madanchian, *J. Data Sci. Intell. Syst.* https://doi.org/10.47852/bonviewJDSIS3202885 (2023).
9. C. Sun, M.H.R. Dehkordi, M.J. Kholoud, H. Azimy, and Z. Li, *Opt. Laser Technol.* 163, 109407 (2023).
10. Y. Yongbin, S.A. Bagherzadeh, H. Azimy, M. Akbari, and A. Karimipour, *Infrared Phys. Technol.* 108, 103364 (2020).
11. B. Peng, et al., *J. Data Sci. Intell. Syst.* https://doi.org/10.47852/bonviewJDSIS3202983 (2023).
12. Z. Li, and S. Li, *CAAI Trans. Intell. Technol.* https://doi.org/10.1049/cit2.12125 (2022).
13. Y.-Q. Wang, J.-Y. Li, C.-H. Chen, J. Zhang, and Z.-H. Zhan, *CAAI Trans. Intell. Technol.* https://doi.org/10.1049/cit2.12106 (2022).
14. K.D. Ramkumar, et al., *J. Manuf. Process.* 16(4), 527–534 (2014).
15. S. Saravanan, K. Raghukandan, and N. Sivagurumanikandan, *J. Manuf. Process.* 25, 284–289 (2017).
16. P. Luchtenberg, P.T. de Campos, P. Soares, C.A.H. Laurindo, O. Maranho, and R.D. Torres, *Surf. Coat. Technol.* 375, 688–693 (2019).
17. L. Pike, *Superalloys* 2008, 191–200 (2008).
18. K. Benyounis, A. Olabi, and M. Hashmi, *J. Mater. Process. Technol.* 164, 978–985 (2005).
19. M. Torkamany, S. Tahamtan, and J. Sabbaghzadeh, *Mater. Des.* 31(1), 458–465 (2010).
20. S. Saravanan, N. Sivagurumanikandan, and K. Raghukandan, *Mater. Today Proc.* 39, 1248–1253 (2021).
21. A. Baghdadchi, V.A. Hosseini, K. Hurtig, and L. Karlsson, *Weld. World* 65, 499–511 (2021).
22. I. Calliari, C. Gennari, E. Hurtado Delgado, A. Miranda Perez, and B. Rodriguez Vargas, *Metal. Ital.* 1(5), 10 (2018).
23. A. Ghosh, P. Kalvettukaran, D. Misra, and S. K. Acharyya, Experimental investigation on the effect of pulse width on laser welding of 2205 duplex stainless steel.
24. H. Gozarganji, A. Farnia, and M. Ebrahimnia, *Arch. Metal. Mater., v*ol. 66, 2021.
25. H. Vemanaboina, G.G. Naidu, G.V. Kumar, and D.R. Reddy, *Mater. Today Proc.* 19, 859–863 (2019).
26. G.N. Ahmad, M.S. Raza, N. Singh, and H. Kumar, *Opt. Laser Technol.* 126, 106117 (2020).
27. M. Azari, E. Rasti, M.H.R. Dehkordi, H. Azimy, A. Zarei, and S.A. Bagherzadeh, *J. Laser Appl.* 33(2), 022015 (2021).
28. P. Thejasree, and P. Krishnamachary, *Mater. Manuf. Processes* 37(10), 1190–1202 (2022).
29. P. Corigliano, and V. Crupi, *Ocean Eng.* 221, 108582 (2021).
30. R.S. Razavi, *Opt. Laser Technol.* 82, 113–120 (2016).
31. S. Kou, Welding metallurgy. *New Jersey, USA* 431(446), 223–225 (2003).
32. K.D. Ramkumar, et al., *Mater. Des.* 68, 158–166 (2015).